Langmuir

ARTICLE

pubs.acs.org/Langmuir

Adsorption and Conformation of Serum Albumin Protein on Gold Nanoparticles Investigated Using Dimensional Measurements and in Situ Spectroscopic Methods

De-Hao Tsai,[†] Frank W. DelRio,[†] Athena M. Keene,[‡] Katherine M. Tyner,[‡] Robert I. MacCuspie,[†] Tae Joon Cho,[†] Michael R. Zachariah,[†,§] and Vincent A. Hackley*[,†]

[†]Material Measurement Laboratory, National Institute of Standards and Technology, Gaithersburg, Maryland 20899-8520, United States

[‡]Center for Drug Evaluation and Research, Food and Drug Administration, Silver Spring, Maryland 20993, United States

[§]Departments of Mechanical Engineering and Chemistry, University of Maryland, College Park, Maryland 20740, United States

S *Supporting Information*

ABSTRACT: The adsorption and conformation of bovine serum albumin (BSA) on gold nanoparticles (AuNPs) were interrogated both qualitatively and quantitatively via complementary physicochemical characterization methods. Dynamic light scattering (DLS), asymmetric-flow field flow fractionation (AFFF), fluorescence spectrometry, and attenuated total reflectance−Fourier transform infrared (ATR-FTIR) spectroscopy were combined to characterize BSA−AuNP conjugates under fluid conditions, while conjugates in the aerosol state were characterized by electrospray-differential mobility analysis (ES-DMA).

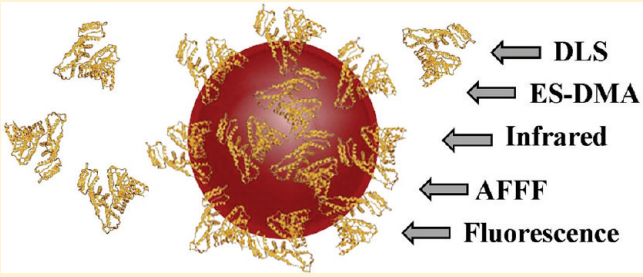

The presence of unbound BSA molecules interferes with DLS analysis of the conjugates, particularly as the AuNP size decreases (i.e., below 30 nm in diameter). Under conditions where the γ value is high, where γ is defined as the ratio of scattering intensity by AuNPs to the scattering intensity by unbound BSA, DLS size results are consistent with results obtained after fractionation by AFFF. Additionally, the AuNP hydrodynamic size exhibits a greater proportional increase due to BSA conjugation at pH values below 2.5 compared with less acidic pH values (3.4−7.3), corresponding with the reversibly denatured (E or F form) conformation of BSA below pH 2.5. Over the pH range from 3.4 to 7.3, the hydrodynamic size of the conjugate is nearly constant, suggesting conformational stability over this range. Because of the difference in the measurement environment, a larger increase of AuNP size is observed following BSA conjugation when measured in the wet state (i.e., by DLS and AFFF) compared to the dry state (by ES-DMA). Molecular surface density for BSA is estimated based on ES-DMA and fluorescence measurements. Results from the two techniques are consistent and similar, but slightly higher for ES-DMA, with an average adsorbate density of 0.015 nm^{-2}. Moreover, from the change of particle size, we determine the extent of adsorption for BSA on AuNPs using DLS and ES-DMA at 21 °C, which show that increasing the concentration of BSA increases the measured change in AuNP size. Using ES-DMA, we observe that the BSA surface density reaches 90% of saturation at a solution phase concentration between 10 and 30 μmol/L, which is roughly consistent with fluorescence and ATR-FTIR results. The equilibrium binding constant for BSA on AuNPs is calculated by applying the Langmuir equation, with resulting values ranging from 0.51×10^6 to 1.65×10^6 L/mol, suggesting a strong affinity due to bonding between the single free exterior thiol on N-form BSA (associated with a cysteine residue) and the AuNP surface. Moreover, the adsorption interaction induces a conformational change in BSA secondary structure, resulting in less α-helix content and more open structures (β-sheet, random, or expanded).

1. INTRODUCTION

The gold nanoparticle−protein conjugate, in which the protein is physically or chemically bound to the surface of a gold nanoparticle (AuNP), has attracted substantial interest in the areas of biodiagnostics and targeted drug delivery for cancer therapeutics.[2−5] The formation of protein conjugates allows for the stabilization of AuNPs over a broad range of pH and ionic strengths and enables the introduction of biologically active functionalities either directly (as part of the protein itself) or via further couplings with the surface-bound protein or underlying gold surface.[6,7] For example, antibody-functionalized AuNPs[8] and tumor necrosis factor (TNF)−conjugated AuNPs[3−5] have been used for targeted cancer therapeutics.

Received: October 13, 2010
Revised: December 14, 2010
Published: February 22, 2011

ACS Publications © 2011 American Chemical Society

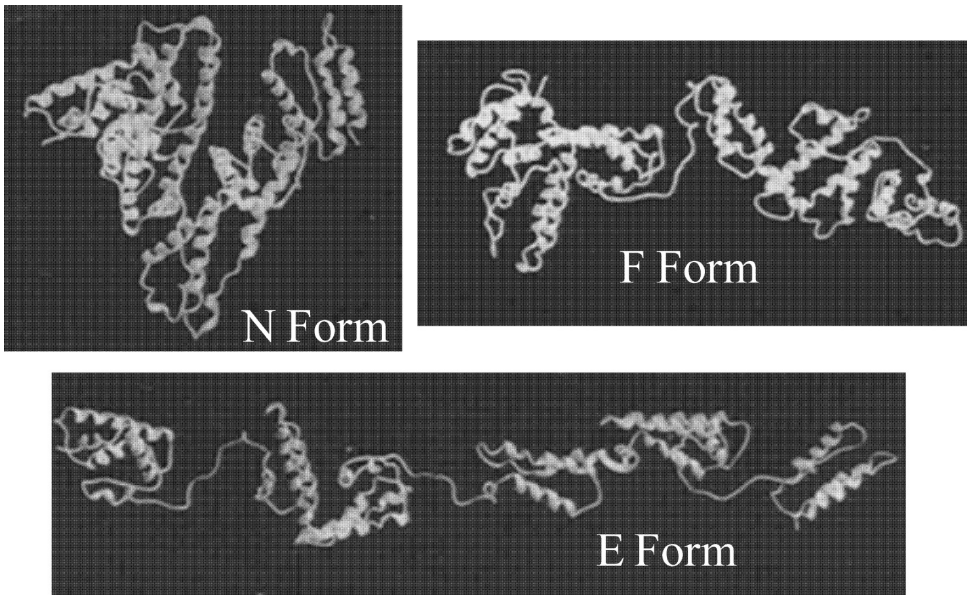

Figure 1. Principal structures of serum albumin: normal conformation (N form, pH 4.5−8), fast conformation (F form, pH 4.5−4), and the fully extended structure (E form, below pH 4). Reproduced with permission from ref 12. Copyright 1994 Elsevier.

Furthermore, upon introduction of nanoparticles into living systems, a protein corona is formed, as serum proteins dynamically associate with the particle surface.[9,10] The presentation of the serum proteins on the particle surface determines the subsequent in vivo response and substantially modifies the nanoparticle dimensions and transport properties, as demonstrated by Dobrovolskaia et al. for AuNPs.[11] Therefore, understanding the interaction between AuNPs and proteins is vitally important for understanding how nanoparticles interact and behave in biological systems.[9,10] This is particularly true for nanomedicine applications, where the regulatory approval required for clinical use sets a high standard for proof of efficacy and safety.

Among the various classes of proteins, albumin (or serum albumin) is conspicuous; it is the most abundant protein in blood, where it is responsible for about 80% of the colloidal osmotic pressure.[12,13] As a multifunctional transport protein, albumin has a broad affinity for many ligands; for instance, albumin acts as a carrier for otherwise insoluble fatty acids in the circulatory system.[14] In addition, albumin plays an important role in the transport and deposition of a variety of substances in therapeutic studies.[12,15−17] Albumin is also chiefly responsible for regulating blood pH.[18] Recently, Porter and co-workers[19,20] proposed using series-specific albumin in combination with a naturally occurring lung fluid surfactant dissolved in phosphate buffered saline (PBS) as a dispersion medium for nanoparticles in the context of in vivo pulmonary toxicity testing. Additional studies have established the general efficacy of albumin proteins as dispersing agents for a range of nanomaterials in different biological media.[21−24] Furthermore, albumin continues to be used as a model protein for many biophysical and biochemical studies.[6,25−27]

Bovine serum albumin (BSA) is the most widely utilized serum protein due to its low cost, wide availability, and structural/functional similarity to human serum albumin (HSA)—having 76% sequence homology[28] and nearly identical pH-dependent conformational transitions.[29] BSA is a water-soluble monomeric protein with a primary structure containing a single polypeptide chain with 583 amino acid residues and a molar mass of 66.4 kDa.[30] The secondary structure purportedly contains roughly 67% α-helix structure with the remainder being random.[12] The tertiary structure consists of nine loops stabilized by 17 internal disulfide bonds between 34 cysteine residues, resulting in three primary domains each containing one small and two large loops.[31] These disulfide bridges are the basis for the compact heart-shaped (equilateral triangle) structure (the so-called N form; see Figure 1)[12] now proposed for BSA in the pH range from 4.5 to 8 as well as providing stability to the helical structure.[31,32] The N form of BSA is characterized by an axial ratio of 2.7, a molecular volume of about 88.25 nm^3, and a radius of gyration or hydrodynamic radius of about 2.6 nm[33] and is slightly negatively charged (though the charge is heterogeneously distributed across the domains).[28] Below pH 4.5, a reversible unfolding occurs that results in the so-called F form, which is characterized by a more elongated shape (roughly 4 nm × 12.9 nm), reduced solubility, and increased viscosity.[34,35] Below pH 4, an additional transition takes place resulting in a fully extended structure (the E form), which is characterized by an aspect ratio of 9.[36] In the N form, only a single free thiol (Cys-34) is accessible on the BSA surface, whereas in the F and E forms, the normally inaccessible disulfides may become accessible to reducing agents or coupling with the AuNP surface.[37] The Cys-34 thiol group is also responsible for the occurrence of dimers in aged BSA solutions.[28] At pH values above 8, another transition occurs resulting in the basic or B form.[12,28]

Even with all that is currently known about native BSA, detailed information on BSA−AuNP conjugates is relatively sparse.[6,7,9,15,38−43] Additionally, a few related studies have examined the adsorption and conformation of BSA onto Au flats.[17,44,45] The structure and behavior of BSA in aqueous solution are governed by multiple interactions, including electrostatic, hydrogen bonding, hydrophobic, and van der Waals. In addition, the reaction of the free thiol on the external surface of

globular (N form) BSA with the AuNP surface could potentially weaken or alter the tertiary or secondary structure of the BSA molecule, which would likely result in the unfolding of BSA from its compact, globular structure.[46] Hence, after binding to AuNPs, BSA may undergo structural changes at the interface, and the resulting less-compact structure may affect BSA's function and bioactivity as well as the stability, reactivity, and transport properties of the AuNP−BSA conjugate. To understand the interactions between BSA and AuNPs, it is therefore necessary to conduct a quantitative investigation requiring complementary and orthogonal characterization techniques. The objective here is to interrogate structural changes in BSA when it interacts with the AuNP surface, to determine BSA surface density, to measure the binding affinity, and finally to determine how the solution environment influences these factors.

Physical characterization methods, such as dynamic light scattering (DLS) and electrospray−differential mobility analysis (ES-DMA), have been utilized in previous studies for the direct characterization of molecular conjugation to nanoparticles.[47−50] The general concept is to measure the increase in particle diameter as a result of ligand adsorption on the AuNP surface. Surface density of conjugated molecules is quantified based on the increase in particle size attributable to the ligands, after accounting for other effects.[48−50] Through the use of an analytical model, the surface density and molecular conformation can be estimated based on the calculated molecular size for different surface densities and measurement environments.

Although physical characterization methods have demonstrated a facile capacity to characterize molecular conjugation on nanoparticles with high speed and resolution,[49−51] an obvious capability gap is that particle size is the only experimental output. For the study of competitive adsorption between two molecules, it is a challenge to differentiate the individual contributions to the particle size arising from each species. In addition, for nanoparticles having a broad size distribution, it is difficult to determine if the increase in particle size is due to molecular conjugation or particle aggregation. Spectroscopic methods[52−54] provide an orthogonal comparison to these physical characterization approaches. By monitoring the change in optical signals corresponding specifically to BSA (absorption or fluorescence), it is possible to track the change in surface density of BSA on AuNPs. One advantage of using spectroscopic methods is to confirm that observed changes in particle size measured by physical methods are in fact due to BSA conjugation and not to particle aggregation. Also, spectroscopic methods provide chemical specificity that allows the study of multiple-adsorbate systems, even when the adsorbates may have a similar physical size.

In the present work, we use DLS to determine particle size and size distribution as a starting point due to the wide availability of this technique.[50,55] DLS is then benchmarked using fractionation techniques: asymmetric-flow field flow fractionation (AFFF) in the wet state and ES-DMA in the dry (aerosol) state. By characterizing the particle size and size distribution using these complementary physical methods, we can probe the formation of BSA surface coatings and analyze its conformation on AuNPs under different environmental conditions. For comparison with the physical characterization methods, fluorescence assay and attenuated total reflectance−Fourier transform infrared (ATR-FTIR) spectroscopy are used to quantify adsorption density of BSA on AuNPs and to evaluate the change in BSA conformation following conjugation.

2. EXPERIMENTAL SECTION

2.1. Materials. Commercially available, 10, 30, and 60 nm citrate-stabilized monodisperse colloidal AuNPs were obtained from Ted Pella Inc. (Redding, CA).[56] The number concentration of particles in solution is estimated to be 5×10^{12}, 2×10^{11}, and 2.6×10^{10} cm^{-3} for nominal 10, 30, and 60 nm AuNPs, respectively. The volumetric ratio (i.e., the volume ratio of AuNP to water) is estimated as 3×10^{-6} for all three nominal sized AuNPs. Highly purified reagent-grade BSA (≥98% protein, ≤ 3 EU/mg endotoxin, fatty acid- and IgG-free, SeraCare Life Science, Milford, MA) was utilized at concentrations ranging from 1.6 to 100 μmol/L. For sample preparation of BSA-conjugated AuNPs, 200 μL of BSA aqueous solutions (0.2−1000 μmol/L) were first prepared and then mixed with 800 μL of AuNPs. Aqueous ammonium acetate (99.9%, Sigma-Aldrich, St. Louis, MO) solution was prepared to adjust the ionic strength (2.5 mmol/L, 0.03 S/m). pH values were measured using an Orion 3 STAR meter (Thermo Electron, Madison, WI) with a InLab semi-microelectrode (Mettler, Teledo, MI). Biological grade 18.2 MΩ·cm deionized water (Aqua Solutions, Jasper, GA) was used for preparing solutions and AuNP suspensions with various concentration factors.

2.2. Dynamic Light Scattering. DLS measurements were performed using a Zetasizer Nano (Malvern Instruments, Westborough, MA). Details of the DLS experimental setup and analysis have been described in previous publications.[47,50] We employ the cumulants method to determine the mean z-average hydrodynamic diameter, $d_{p,hz}$, and the polydispersity index (PI); for additional information and experimental details refer to section 8.1 of the Supporting Information. The DLS instrument used in this study was operated in both batch and online (flow) mode, the latter in conjunction with AFFF fractionation (see below).

2.3. Electrospray−Differential Mobility Analysis (ES-DMA). The ES-DMA system consists of an electrospray aerosol generator (model 3480, TSI Inc., MN), a differential mobility analyzer (DMA, model 3080n, TSI Inc.), and a condensation particle counter (CPC, model 3025, TSI Inc.). Details of the ES-DMA experimental setup have been described in previous publications.[48,49,54,57−59] Additional experimental details are summarized in section 8.2 of the Supporting Information.

2.4. Asymmetric−Flow Field Flow Fractionation (AFFF). The AFFF system consists of a high-performance liquid chromatography (HPLC) isocratic pump (1100 series, Agilent Technologies, Santa Clara, CA), manual injection valve (Rheodyne 7725i, IDEX Corporation, Oak Harbor, WA) with a 100 μL stainless steel sample loop, field/flow control module, and AFFF separation channel (Eclipse 2, Wyatt Technology, Santa Barbara, CA), multiangle light scattering (MALS) detector (Dawn Heleos, Wyatt Technology), and ultraviolet−visible (UV−vis) absorbance diode array detector (1200 DAD, Agilent Technologies). The instrument configuration uses a DLS device operated in flow mode as the final detector (Zetasizer Nano, Malvern Instruments Inc.). Details of the AFFF experimental setup have been described in a previous publication.[60] Finally, the particle size corresponding to an eluting peak can be calibrated in situ by flow mode DLS measurements. For a summary of the method and additional experimental details, refer to section 8.3 of the Supporting Information.

2.5. Attenuated Total Reflectance−Fourier Transform Infrared (ATR-FTIR) Spectroscopy. ATR-FTIR spectroscopy was performed using a Nicolet Spectra 750 FTIR equipped with a Thunder Dome Germanium ATR accessory (Thermo Scientific, Madison, WI). Spectra were collected from an average of 128 scans with a resolution of 1 cm^{-1}. For sample preparation, 800 μL of as-received AuNP solution was first concentrated 16× by centrifugation and then drop-cast onto the surface of the germanium crystal. After evaporating the solvent in a clean bench at room temperature (21 °C), a AuNP film

was formed on the crystal surface (roughly 300 nm in thickness). Then, a flow cell unit (Thermo Scientific) was attached to the top of the crystal in order to allow fluid to contact and penetrate the AuNP film. The background spectra were recorded by introducing deionized (DI) water into the flow cell. BSA solutions under various experiment conditions (e.g., pH, BSA concentration) were then introduced into the flow cell, and the resulting spectra were recorded.

2.6. Fluorescence Spectrometry. Fluorescence spectrometry was conducted using a Quant-iT protein assay kit (Invitrogen, Paisley, UK). The assay involves a dye that fluoresces when bound to the detergent coating and/or hydrophobic regions of proteins, while the unbound dye is not fluorescent. First, 200 μL of the working solution, containing the fluorescent dye and the protein buffer, was loaded into each microplate well, and then 5−20 μL test samples of the AuNP−BSA were added into each well so that the fluorophore could bind to the protein. BSA standards (10 μL) with concentrations in the range 25−500 ng/μL were placed in separate wells to facilitate quantitative calibration. A SAFIRE multidetection monochromator microplate reader (Tecan Inc., Durham, NC) was employed for the fluorescence measurements. The excitation wavelength was 470 nm, and the fluorescence was measured at 570 nm.

Through use of calibration with standards, the amount of BSA presenting in AuNP samples can be quantified based on the corresponding fluorescence intensity, I_f. For the concentration range we cover, the amount of BSA presenting in each well can be calculated using a correlation of $(I_f + 28)/0.4833$ (expressed as 10^{-9} g of BSA).

2.7. Measurement Uncertainty. Error bars shown in figures and uncertainty ranges associated with measurement values represent one standard deviation calculated from replicate (2−4) measurements performed under repeatability conditions.

3. RESULTS AND DISCUSSION

3.1. Physical Characterization of BSA Conjugation on AuNPs in the Wet State. DLS was used to characterize the hydrodynamic size, $d_{p,hz}$, of AuNPs before and after BSA conjugation. The non-negative least-squares (NNLS) regularization algorithm has been applied widely for calculating particle size distributions from DLS data (Figure S1, Supporting Information). However, because of the lack of standardization for NNLS and other inversion algorithms, the cumulants approach was chosen for the analysis of DLS data in this study.[61,62]

As shown in Figure 2a for nominally 10 nm AuNPs, following conjugation with BSA the correlation function, $G(\tau)$, exhibits a nonlinear decay (i.e., a significant secondary coefficient μ_2 is evident); this indicates an increase in the variance of particle diffusion coefficients (or PI) relative to the native particles and suggests increased polydispersity in size. When the nominal (core) size is increased to 60 nm (Figure 2b), the correlation decay becomes nearly linear (i.e., μ_2 decreases with increasing particle size), indicating that the PI does not increase following BSA conjugation and suggesting an absence of agglomeration. From the first-order coefficient, $\overline{\Gamma}$, obtained from data shown in Figure 2a,b, $d_{p,hz}$ was calculated. Here the amount of BSA presenting in solution is at least 1000 times higher than the required amount to have a maximum monolayer surface coverage.[6,27,63] Figure 2c summarizes the change in $d_{p,hz}$ (denoted $\Delta d_{p,hz}$) and PI (denoted ΔPI) as a function of the native (core) diameter. As the core size increases, $\Delta d_{p,hz}$ increases while ΔPI decreases. Note also that $\Delta d_{p,hz}$ is close to zero for the smallest core size, even though the PI increases following conjugation. If agglomeration were occurring, both $\Delta d_{p,hz}$ and PI should increase. Similarly, if conjugation were occurring in a heterogeneous manner (i.e., more BSA adsorption on some particles and less on others), both $\Delta d_{p,hz}$ and PI should increase, though relatively less so than would be expected for agglomeration effects. We have also observed that $\Delta d_{p,hz}$ exhibits a dependence on the concentration factor (i.e., the number concentration of AuNPs used in experiments compared to the as-received particle concentration). As shown in Figure 2d, a negative $\Delta d_{p,hz}$ (≈ -1 to -5 nm) was observed for nominally 10 nm AuNPs at all dilution levels; the variation in the measurement results versus concentration factor can be attributed primarily to the fitting uncertainty in the autocorrelation function (Supporting Information, eq S1). For nominally 30 nm AuNPs, increasing the concentration factor increases $\Delta d_{p,hz}$ significantly from -9.6 to 8.5 nm. For nominally 60 nm AuNPs, increasing the concentration factor increases $\Delta d_{p,hz}$ from 7.3 to 11.4 nm, which indicates that the concentration factor is less significant as compared to the two smaller size AuNPs. Similar to the results in Figure 2c, a larger ΔPI value was observed when $\Delta d_{p,hz}$ was close to zero or negative. Finally, it is important to note that the concentration factor does not have a significant impact on either $\Delta d_{p,hz}$ or ΔPI for unconjugated AuNPs over the range studied here.

On the basis of the above arguments, we conclude that the dependencies on the core size and particle concentration factor results from the presence of unbound globular BSA molecules. The free BSA apparently contributes sufficiently to the measured correlation function to interfere with measurement of the AuNPs (i.e., convolution of scattering from both species impacts the cumulants determination of the mean z-average size); this effect is noticeable for AuNP core sizes as large as 30 nm, whereas for the 60 nm cores the particle scattering dominates the correlation spectrum sufficiently and the effect of free BSA is insignificant.

The BSA interference can be analyzed assuming Rayleigh scattering properties, in which the scattering intensity is proportional to $N_p d_{p,hz}^6$. The hydrodynamic diameter of a BSA monomer, $d_{BSA,hz}$, has been reported or estimated to be about 4.2−7 nm,[31,51,64−66] which is comparable to the 10 nm AuNPs used in our experiments. In addition to $d_{BSA,hz}$, the number of free BSA molecules in solution, N_{BSA}, is at least 10^4 times the population of AuNPs, N_p. Hence, the light scattering intensity from unbound BSA can be significant compared to the scattering intensity from AuNPs, especially for particles having smaller core size (i.e., 10 nm AuNPs). When d_{p0} increases to 60 nm, the artifact resulting from the free BSA is negligible.

To quantify the impact of the free BSA on the scattering measurement, we define a dimensionless parameter

$$\gamma = \frac{\text{AuNP scattering intensity}}{\text{BSA scattering intensity}} = \frac{\varepsilon_p N_p d_{p0}^6}{\varepsilon_{BSA} N_{BSA} d_{BSA}^6} \quad (1)$$

where ε_p and ε_{BSA} are the refractive index for AuNPs and BSA, respectively. In this study, we used $\varepsilon_p = 0.47$[67] and $\varepsilon_{BSA} = 1.445$.[41] $d_{p0,hz}$ is the hydrodynamic diameter for unconjugated Au-NPs. With an increase in γ, the impact from free BSA decreases, and therefore the accuracy of $\Delta d_{p,hz}$ improves. For example, the molar mass (M) of 5 kDa thiolated poly(ethylene glycol) (SH-PEG5K) is 13× smaller than a BSA monomer; therefore, the scattering intensity from unbound SH-PEG5K should be 170× lower than that from BSA at the same solution concentration. Hence, the contribution from the unbound SH-PEG5K is negligible for AuNPs used in the previous study.[50]

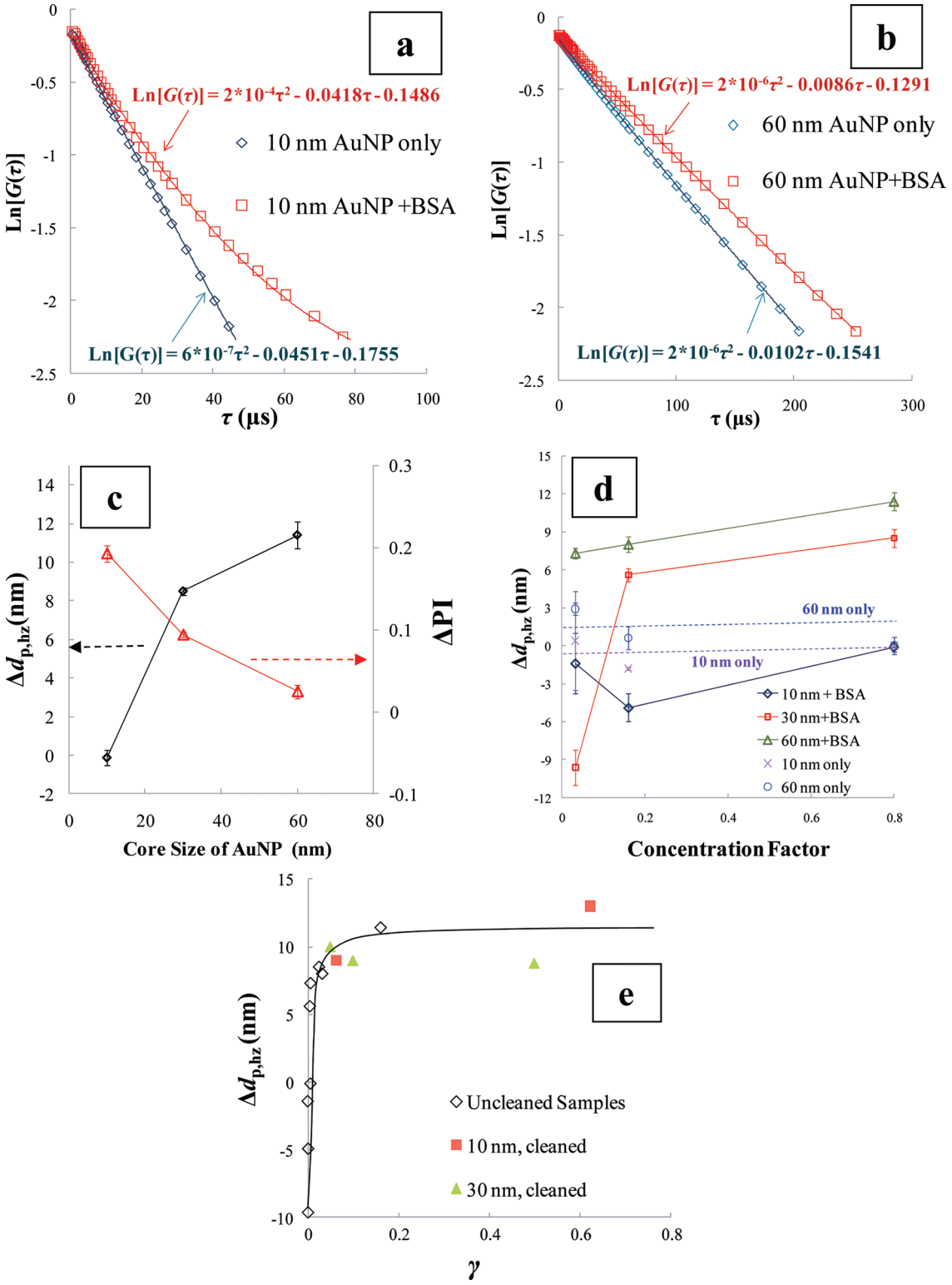

Figure 2. Characterization of BSA conjugation on AuNPs by DLS. (a) Cumulant analysis, 10 nm AuNPs with 100 μmol/L of BSA. (b) Cumulant analysis, 60 nm AuNPs with 100 μmol/L of BSA. (c) Effect of AuNP core size on $\Delta d_{p,hz}$ and ΔPI without centrifuge treatment. Concentration of AuNPs is 80% of the as-received concentration (concentration factor = 0.8). C_{BSA} is 100 μmol/L. The solid line is to guide the eyes. (d) Effect of particle concentration on $\Delta d_{p,hz}$. Different concentration factors for AuNPs with 100 μmol/L of BSA. Two reference data sets (10 and 60 nm cores without BSA) were used to show $\Delta d_{p,hz}$ vs concentration factor without BSA conjugation. The solid line is to guide the eyes. (e) $\Delta d_{p,hz}$ versus γ; the centrifuged samples were at a concentration factor of 0.8, and the uncentrifuged samples represent different nominal core sizes (10, 30, and 60 nm, open diamonds) and concentration factors. pH of samples ranged from 6.0 to 7.9. The solid line fit for open diamonds (no centrifugation) in (e) is to guide the eyes. Data points are the mean values of at least four replicate measurements, and error bars (smaller than the symbol size) represent one standard deviation.

Table 1. Summary of the Change of Particle Size and ΔPI Measured by DLS and ES-DMA

nominal AuNP size (nm)	$d_{p0,hz}$ (nm)	$d_{p0,m}$[a] (nm)	$\Delta d_{p,hz}$, with BSA (nm)	$\Delta d_{p,hz}$, with BSA + cleaning (nm)	$\Delta d_{p,m}$,[a] with BSA (nm)	ΔPI, with BSA (nm)	ΔPI, with BSA after cleaning (nm)
10	13.8 ± 0.5	13.0 ± 0.1	−2.0 ± 2.5	13.2 ± 0.2	6.3 ± 0.1	0.193 ± 0.01	−0.089 ± 0.043
30	30.4 ± 0.1	31.1 ± 0.3	8.5 ± 0.7	8.3 ± 0.2	6.1 ± 0.3	0.094 ± 0.003	0.036 ± 0.015
60	58.2 ± 0.4	59.0 ± 0.3	11.4 ± 0.7	11.5 ± 1.1	5.9 ± 0.3	0.025 ± 0.008	0.012 ± 0.013

[a] Uncertainty was determined from a previous study.[49]

Figure 2e summarizes the correlation between $\Delta d_{p,hz}$ and γ. The role of γ in Figure 2e is to serve as an indicator with regards to selecting suitable conditions for conducting DLS measurements in the AuNP-BSA system. The γ values of the centrifuged samples are calculated based on the amount of supernatant (containing excess BSA) removed in the centrifugation process, assuming no particle loss during centrifugation (e.g.: γ is increased 20× if replacing 950 μL supernatant from 1000 μL of Au colloids). The open diamond symbols represent the data of precentrifuged samples for three different core size Au-NPs, whereas the solid line fitted through the open diamonds is used to guide the eyes. Clearly, $\Delta d_{p,hz}$ reaches a plateau when $\gamma > 0.1$; in order to mitigate the artifact from the unbound BSA molecules, γ should be at least 0.1. For smaller AuNPs with a lower particle concentration, removing the unbound BSA molecules by centrifugation and supernatant replacement can improve γ. As shown in Figure 2e, using the centrifugation approach, $\Delta d_{p,hz}$ for both 10 and 30 nm AuNPs increases and becomes nearly coincident with $\Delta d_{p,hz}$ for 60 nm AuNPs that have not been centrifuged: $\Delta d_{p,hz}$ is 13.2 and 8.3 nm for 10 and 30 nm, respectively. Table 1 summarizes the change of particle size and ΔPI of AuNPs before and after conjugating with BSA. Note that the negative values for $\Delta d_{p,hz}$ observed in Figure 2c,d arise from an artifact of the cumulants analysis. In this case, the contribution to the correlation decay associated with the unbound BSA is averaged with the principal correlation decay of the BSA-conjugated AuNPs leading to an apparent decrease in size for the AuNPs. This artifact is eliminated when the unbound BSA is removed, for instance, by centrifugation.

In order to confirm $\Delta d_{p,hz}$ values determined by batch-mode DLS and to rule out other potential effects such as agglomeration, we employed AFFF to fractionate test samples prior to online analysis. In addition to fractionation and size determination (based on retention time), on-board UV−vis absorption spectroscopy, multiangle light scattering (MALS), and flow-mode DLS detectors permit differentiation of components by size and chemical speciation. In Figure 3a, nominally 60 nm AuNPs were chosen to exemplify the method, though it should be applicable to other particle sizes, including nominally 10 and 30 nm AuNPs.[60] After converting retention time to equivalent spherical hydrodynamic size, the fractograms measured by AFFF for nominally 60 nm AuNPs, with and without BSA, are shown in Figure 3a. The corresponding UV−vis spectra obtained at the peak positions denoted 1 to 4 in Figure 3a are shown in Figure 3b. Note that the concentration factor used for AFFF measurements was 0.08 for 60 nm AuNPs.

Three modes (peaks) were observed in the MALS trace (measured at 90°) for BSA-conjugated AuNPs, which contain both bound and free BSA. This trace should be compared with the MALS trace for native (preconjugation) AuNPs, also shown in Figure 3a. The small mode identified as peak 1 in Figure 3a, located at ≈5 nm ($t_r - t_0 = 2.9$ min, void peak at t_0 is not shown)

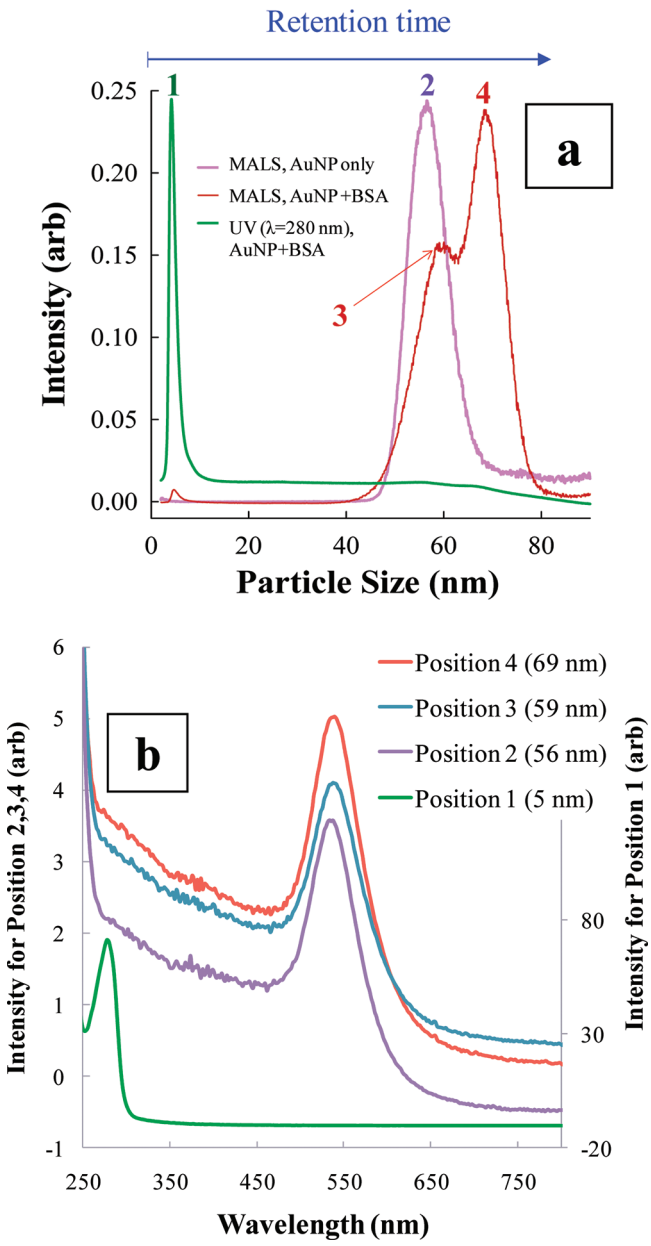

Figure 3. Characterization of BSA conjugation on nominal 60 nm AuNPs using AFFF. (a) MALS and UV (λ = 280 nm) traces for AuNPs. (b) UV−vis spectra obtained online at specific points identified in (a). C_{BSA} is 100 μmol/L, the concentration factor is 0.08, and pH is 6.7. Void peaks are not shown in the figure.

in both the UV trace and the MALS trace, is attributed to unbound BSA (the maximum absorption wavelength, λ_{max}, occurs at 276 nm). The peaks located between 59 and 67 nm

(peak 2 for native AuNPs, peaks 3 and 4 for BSA−AuNPs) are assigned to AuNPs; these peaks eluted from $t_r - t_0$ = 31 to 37 min, respectively. The corresponding UV−vis spectra (Figure 3b) for peaks 2−4 exhibit classic surface plasmon resonance bands for AuNPs in this size range ($\lambda_{max} \approx 530$ nm). Moreover, although the MALS trace for BSA-conjugated AuNPs shows a doublet (peaks 3 and 4 in Figure 3a), the corresponding UV−vis spectra (with $\lambda_{max} \approx 530$ nm), as well as online DLS measurements ($d_{p,hz} \approx 66$ nm as measured by Malvern Nano ZetaSizer, not shown in Figure 3), are virtually identical for peaks 3 and 4, suggesting these features represent a single species that is 66 nm in diameter (i.e., BSA−AuNPs). We attribute the peak splitting phenomenon to particle−membrane interactions, which are beyond the scope of the present work. However, this serves to emphasize the importance of combining multiple sensing or detection methods in order to accurately identify and characterize complex systems that may contain or exhibit multiple components, whether real or artifact. The increase in particle size, $\Delta d_{p,hz}$, based upon results from the online DLS is 9.3 ± 0.3 nm, which is close to the value obtained in batch mode DLS (see Figure 2). This confirms the homogeneous BSA conjugation to the surface of AuNPs.

3.2. Effect of pH on the Molecular Conformation of Adsorbed BSA. As stated previously (Figure 1), BSA undergoes conformational expansion from the heart-shaped N form (see Figure 1) that is associated with pH values above its isoelectric point (≈4.7) to more elongated and open structures (F and E forms) at pH values below its isoelectric point.[12,32] Since a wide range of pH values may be encountered in biological systems (e.g., ranging from about pH 1.5 to 3.5 in the human stomach to pH 4.7 in lysosomes and pH 7.4 in human blood), it is clearly important to understand the effect this will have on the structure and stability of surface-bound BSA, as this will likely impact AuNP conjugate properties and interactions. Presently, this area remains largely unexplored,[25,68] especially in the use of direct physical characterization of surface-bound BSA. Much more work has been reported regarding the conformation of free (unbound) BSA.[12,28,31,34,36,46,69] Relevant to the present study, Kun et al.[69] employed DLS over various pH conditions and were able to demonstrate a larger hydrodynamic size for the E form than the N form. Li et al.[70] examined the conformation of BSA as a function of pH adsorbed at a flat gold surface using force microscopy and small-angle neutron scattering; their findings indicated that the conformation of BSA conjugates is more compact when the pH is close to the isoelectric point of native BSA (4.7).[12,28] To provide direct information on the conformation of BSA adsorbed to AuNPs, we will utilize DLS to characterize the change of hydrodynamic size of the BSA conjugates over a broad range of pH values.

In order to simplify measurement conditions, experiments were conducted using nominally 60 nm AuNPs, since the high γ value precludes having to remove the unbound BSA prior to DLS measurements. First, eight samples of BSA conjugated AuNPs were prepared at pH 7.3, C_{BSA} =10 μmol/L. Then these samples were titrated with nitric acid to their targeted pH values and measured by DLS within 1 h after pH adjustment. DLS results for the BSA−AuNP conjugates as a function of solution pH are shown in Figure 4a. Size is represented as the change in half of the hydrodynamic diameter, $0.5\Delta d_{p,hz}$ (i.e., the presumed shell thickness), relative to the unconjugated AuNPs (determined under stable conditions near pH 7). The results indicate a single sharp transition between two stable size regimes, while the PI remains relatively unchanged over the entire pH range tested

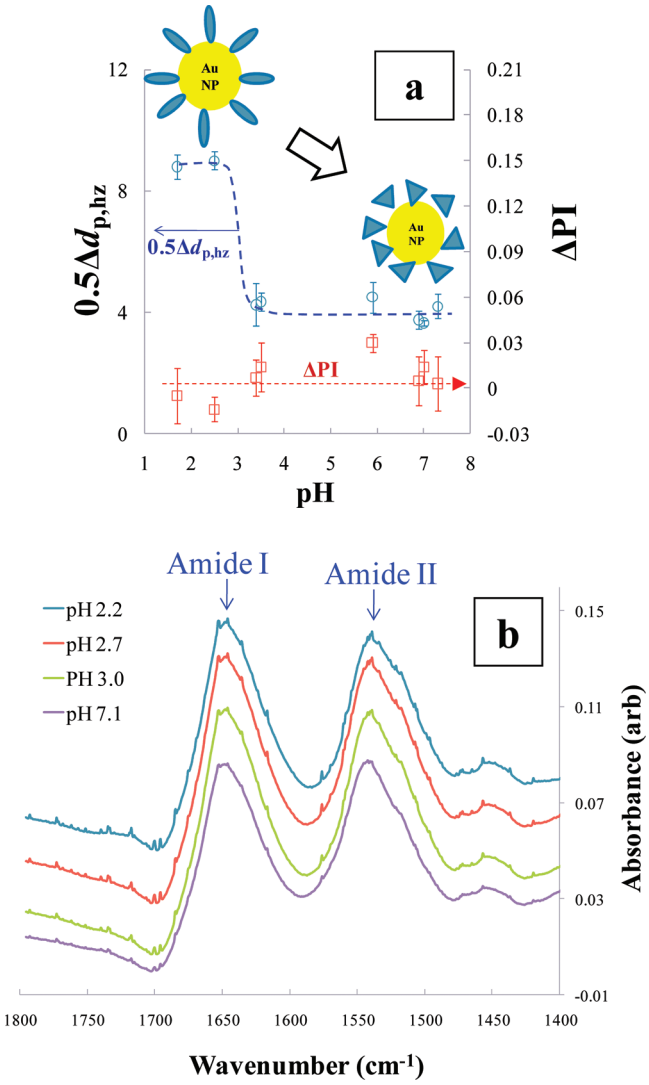

Figure 4. Effect of pH on the surface conformation of BSA conjugates on nominal 60 nm AuNPs. (a) $0.5\Delta d_{p,hz}$ and ΔPI as a function of pH. Data were recorded within 1 h of adjusting pH. Note that pH values were measured directly on the DLS samples. C_{BSA} is 10 μmol/L. Data points are the mean values of four measurements, and error bars are one standard deviation. Lines are included for visual guidance. (b) ATR-FTIR spectra for BSA−AuNP conjugates as a function of decreasing pH (from bottom to top). C_{BSA} is 10 μmol/L. Spectra are vertically shifted for the purpose of clarity.

(ruling out agglomeration effects, but not multilayer adsorption). Below about pH 2.7 a thicker or more vertically aligned layer of BSA increases the hydrodynamic size of the conjugate, while above pH 3.4 and up to physiological pH the hydrodynamic size remains stable and relatively smaller. The results are consistent with a transition between the N form and either the F or E form of free BSA but also suggest some conformational inhibition (i.e., lower transition pH) relative to free BSA due to attachment on the Au surface; the N−F transition for free BSA occurs above pH 4. So it is plausible that conjugated BSA exhibits only a single conformational transition, though we may simply not be able to resolve the transition from F to E based on DLS measurements alone. Another possibility is that the surface binding process between BSA and Au-NPs may itself induce conformation

changes, similar to the N−F transformation, even in the so-called N form pH regime.[12,25] Hence, the transition between N and F forms becomes less observable.

To rule out the effect of possible differences in surface density or the occurrence of multilayers, we evaluated the effect of pH on BSA adsorption using ATR-FTIR. This analytical approach is surface sensitive due to the limited penetration of the evanescent wave, which preferentially samples material deposited directly onto the ATR crystal and is therefore less affected by the composition of the bulk solution. Since a relatively dense layer of AuNPs can be placed on the crystal surface, the interfacial-to-bulk ratio can be maximized. Initially, a solution of 10 μmol/L BSA was introduced to an immobilized AuNP film at neutral pH to obtain surface saturation under N-form conditions. Then, a 10 μmol/L BSA solution preadjusted to different pH values was flushed through the ATR cell and allowed to equilibrate for 5 min before acquiring each spectrum. Figure 4b shows the spectra of BSA conjugates on AuNPs as a function of pH. Spectra are vertically adjusted for the purpose of clarity. The two adsorption bands are indicative of amide groups: amide I (1600−1700 cm^{-1}) and amide II (1500−1600 cm^{-1}).[71−73] The amide I region is mainly due to C=O stretching, while the amide II region reflects in-plane N−H bending and C−N stretching. In general, amide II is less sensitive to protein conformation changes (secondary or tertiary structure) but is useful for quantification of protein adsorption in aqueous solution due to its reduced interference from the absorbance of molecular water (≈1640 cm^{-1}) relative to amide I. Over a range of pH values from 2.2 to 7.1, as shown in Figure 4b, the peak height of the IR absorbance for the amide II band is nearly constant (the peak height of absorbance is 0.07 ± 0.006), indicating that molecular surface density is relatively unchanged in this pH range. This supports the supposition that the transition in $0.5\Delta d_{p,hz}$ observed in Figure 4a is primarily due to a change in adsorbed BSA conformation. In section 3.6 we will continue to use IR to investigate the effect of pH on the secondary structure of BSA. In addition to pH, we examined the influence of ionic strength on BSA structure over the range represented in the investigation reported here and found no observable dependence of *z*-average size (Supporting Information, Figure S3).

3.3. Characterization of BSA Conjugation on AuNPs in the Dry State. The number-weighted particle diameter, $d_{p,m}$, of conjugated and unconjugated AuNPs in the dry state (i.e., as aerosols) was obtained using ES-DMA. Figure 5a−c summarizes the ES-DMA results and clearly illustrates a significant increase in $d_{p,m}$ (defined as $\Delta d_{p,m}$) following conjugation with BSA, even in the dry state. For nominally 10 nm AuNPs, the mean $d_{p,m}$ increases from 13.0 to 19.3 nm ($\Delta d_{p,m}$ = 6.3 nm). For 30 nm AuNPs, the mean $d_{p,m}$ increases from 31.1 to 37.2 nm ($\Delta d_{p,m}$ = 6.1 nm), and for 60 nm AuNPs, the mean $d_{p,m}$ increased from 59.0 to 64.9 nm ($\Delta d_{p,m}$ = 5.9 nm). Thus, as the core size decreases, $\Delta d_{p,m}$ exhibits a slight increasing trend. The reason may be due to differences in BSA surface density as will be discussed in a later section. As shown in Table 1, the uncertainty in the mean diameter determined by ES-DMA measurements is significantly lower (≈0.3 nm) than $\Delta d_{p,m}$ resulting from BSA conjugation (≈6 nm), confirming that $\Delta d_{p,m}$ determined from the distributions in Figure 5 is statistically significant.

Because ES-DMA is a particle counting technique with high resolution, the number-weighted distribution generated by ES-DMA should be able to accurately reflect the actual distribution or spread in particle size.[49,59,74,75] From the change in distribution width, we can draw some conclusions concerning the homogeneity of the molecular conjugation. Applying a core−shell model to the BSA−AuNP conjugates,[48−50] the full width at half-maximum (fwhm) of the size distribution[76] should increase only if conjugation is heterogeneous (i.e., varies across different particles) or if coated and uncoated particles coexist in the particle population following conjugation with BSA. Conversely, if a uniform coating is formed, the width of size distribution should be conserved following conjugation, though the peak itself should shift upward.[48−50] As shown in Figure 5a−c, following conjugation with BSA, the fwhm were relatively unchanged for the three core sizes, indicating the formation of a homogeneous BSA shell over the AuNP core. In addition, the size distributions measured by ES-DMA show a single normal (Gaussian type) peak (i.e., no peak splitting or multimodal distribution), confirming the splitting shown in the AFFF data in Figure 3a is not attributable to heterogeneous (bimodal) BSA surface density or aggregation of AuNPs but is likely a measurement/fractionation artifact as previously suggested.

In comparing the increase in particle size due to BSA conjugation in different environments, we find that the increase in size measured in the dry state ($\Delta d_{p,m}$) is about 6 nm; this value is significantly lower than $\Delta d_{p,hz}$ measured in solution (≈ 8−12 nm by DLS and AFFF). This is consistent with our previous results for SH-PEG5K on AuNPs.[50] In solution, the particle size measured by DLS or AFFF represents the hydrodynamic envelope of the particle−molecule conjugate presented as an equivalent sphere and is relatively less affected by the surface density in the monolayer regime. That is, a submonolayer of adsorbed protein, extending out from the surface and sweeping entrapped solution along with it as it diffuses, will greatly increase the hydrodynamic size relative to the native particle; further addition of protein toward a full monolayer will contribute minimally to the hydrodynamic envelope, as it tends to simply fill in gaps and does not further extend the envelope. On the other hand, $\Delta d_{p,m}$ measured in the dry state should be less than that measured in the wet state because solvent is removed and the protein is collapsed onto the surface during the ES-DMA analysis. Current results bear this out. In addition, it is found that BSA has a more compact conformation than SH-PEG5K; the ratio $\Delta d_{p,m}/\Delta d_{p,hz}$ for BSA−AuNPs is much larger (48−75%) relative to $\Delta d_{p,m}/\Delta d_{p,hz}$ for SH-PEG5K−AuNPs (≈25%).[50]

3.4. Quantification of Adsorbed Density. One advantage of ES-DMA is its capacity to quantify molecular surface density under certain conditions.[48−50] To accurately convert $\Delta d_{p,m}$ obtained by ES-DMA to the number of molecules attached to the surface of AuNPs, it is important to have a constant molecular size during the measurements. However, as previously shown, BSA is known to undergo conformational changes with environmental variations (e.g., pH and ionic strength) while in the wet state. Moreover, conformational changes observed during solution phase measurements (i.e., by DLS) make it difficult to quantify surface density based on size increase alone. On the other hand, measuring the size change in the dry state avoids the convolution of surface density and conformation in the wet state, since interactions with the solution phase are removed during the aerosolizing process. Hence, the physical size of BSA can be assumed constant during the ES-DMA measurements, regardless of the solvent conditions used prior to analysis.

Since ES-DMA can be used to accurately measure the particle size of BSA-conjugated AuNPs with very high resolution and

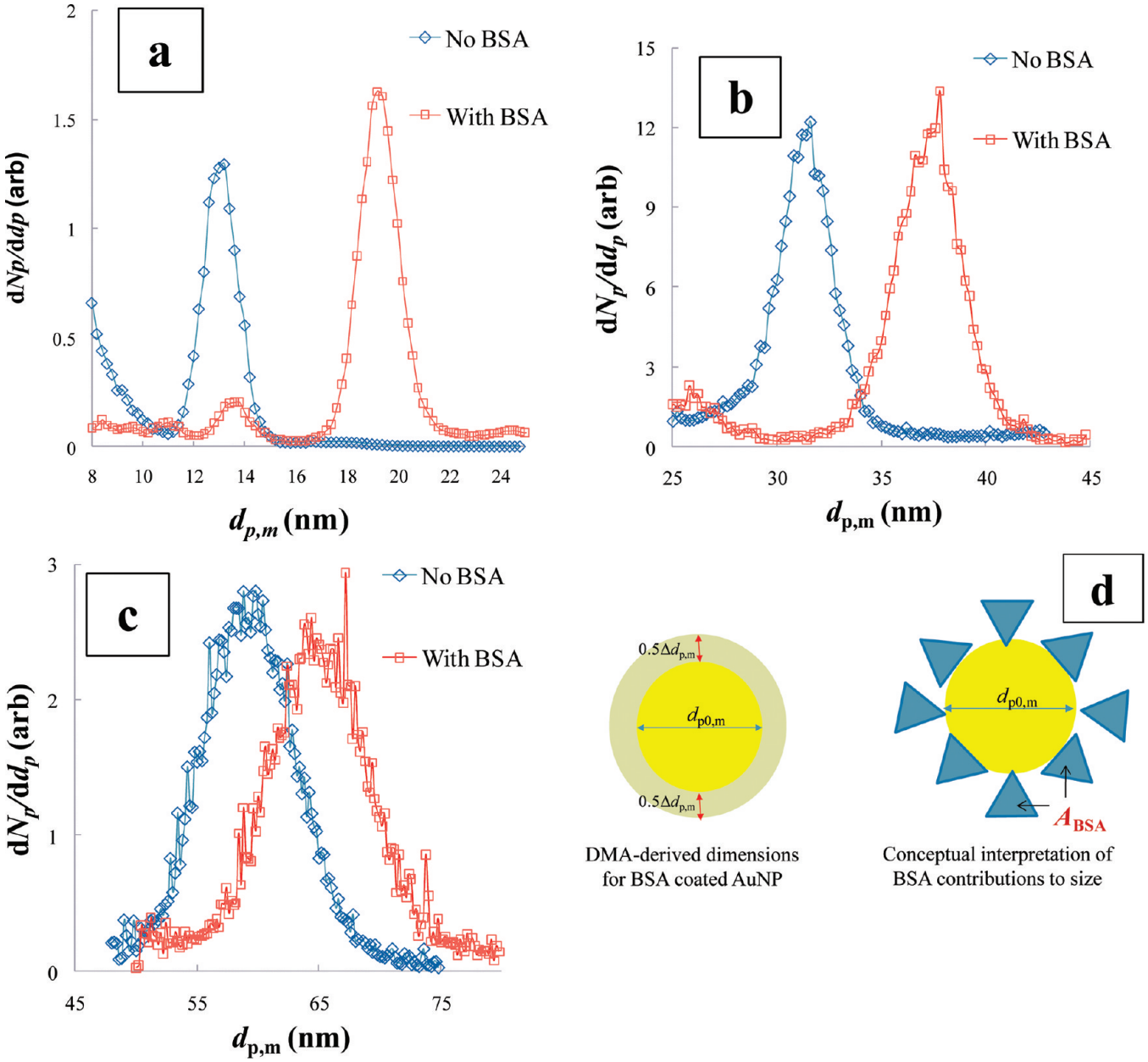

Figure 5. Quantification of BSA conjugation on AuNPs by ES-DMA. (a) Particle size distributions of nominally 10 nm AuNPs. (b) Particle size distributions of nominally 30 nm AuNPs. (c) Particle size distributions of nominally 60 nm AuNPs. (d) Conceptual model for the calculation of molecular surface density via ES-DMA. C_{BSA} was 100 μmol/L, and the experiment was conducted at pH 7.

based on particle surface-to-charge ratio, the quantity of BSA molecules conjugated to AuNPs can be estimated from $\Delta d_{p,m}$.[48−50] A conceptual analytical model is shown in Figure 5d. From the increase in cross-sectional area of AuNPs, ΔA, the molecular surface density of BSA on AuNPs, σ, can be obtained via[48,49]

$$\Delta A = \pi[(d_{p0,m} + \Delta d_{p,m})^2 - d_{p0,m}{}^2]/4 = NA_{BSA} \qquad (2)$$

Here, $d_{p0,m}$ is the diameter of core AuNPs measured by ES-DMA, and A_{BSA} is the cross-sectional area of BSA molecule. Using an equilateral triangular model for globular N-form BSA with 8 nm edges and 3 nm thickness,[31] $A_{BSA} \approx 25.9$ nm^2 (details of calculation of A_{BSA} are included in the Supporting Information). N is the number of BSA molecules attached to the cross-sectional perimeter of the AuNPs ($\pi d_{p0,m}$) and $N = N_m \pi d_{p0}$. N_m is the linear molecular density around the two-dimensional projection of the particles' circumference,[48] which can be used to calculate σ (where $\sigma = N_m{}^2$). Substituting N in eq 2, σ can be expressed as

$$\sigma = \frac{[(d_{p0,m} + \Delta d_{p,m})^2 - d_{p0,m}{}^2]^2}{[4d_{p0,m}A_{BSA}]^2} \qquad (3)$$

Using $\Delta d_{p,m}$ and $d_{p0,m}$ measured in Figure 5a−c, the surface density of BSA, σ, is found to be 0.023 ± 0.003 nm^{-2} for nominal 10 nm AuNPs, 0.017 ± 0.002 nm^{-2} for nominal 30 nm AuNPs, and 0.014 ± 0.002 nm^{-2} for nominal 60 nm AuNPs. These values correspond to 12, 52, and 153 molecules/particle for nominally 10, 30, and 60 nm AuNPs, respectively. Thus, the

maximum surface density measured by ES-DMA ranges from ≈34% to ≈60% of the maximum monolayer surface density, $\approx 1/A_{BSA}$ (0.0386 nm^{-2}, assuming no spacing between BSA conjugates). The apparent submonolayer density could be attributed to intermolecular electrostatic repulsion and also steric hindrance between adsorbed BSA occupying neighboring sites on the Au surface. Modeling this "jamming effect" (i.e., space-limiting due to the mutual repulsion between adsorbed BSA molecules) has been shown to decrease the surface density as much as 71% of the maximum monolayer density depending on the molecular dimension used for the model.[77,78] Note that the core−shell model (eq 3) is applicable for the calculation of σ when the number of adsorbate molecules attached to the AuNP is extensively higher than unity. If the core size is less than about 10 nm, a heterogeneous aggregation model may be more appropriate, but this is beyond the scope of the present work.

Fluorescence spectrometry was used for semiquantitative comparison and confirmation of the ES-DMA results. An advantage of using fluorescence is that surface density can be determined using the same suspension measured by ES-DMA. Because more than 99.98% of unbound BSA was removed from the AuNP samples, the fluorescence signals, and the corresponding BSA concentration, can be mostly attributed to the BSA bound to AuNPs. Knowing the total surface of AuNPs, σ based on fluorescence can be obtained with the corresponding fluorescence signals.

As measured, σ based on fluorescence is determined to be 0.010 ± 0.005 nm^{-2} for nominal 30 nm AuNPs and 0.008 ± 0.002 nm^{-2} for nominal 60 nm AuNPs. Because of poor recovery of AuNPs following the required centrifugation cleaning process, surface density for nominal 10 nm AuNPs appears unrealistically low (0.005 ± 0.001 nm^{-2}) and is therefore considered unreliable. Similar recovery issues were observed in the processing of samples for ES-DMA, but in this case results are not dependent on recovery. Nevertheless, in general, the surface density measured by ES-DMA is of the same order of magnitude as the results by fluorescence spectrometry. In addition, the results are consistent with reported values for BSA on Au surfaces, ranging from 0.015 to 0.03 nm^{-2}.[6,27,63]

The ES-DMA and fluorescence results suggest a dependence of surface density (or adsorption) on particle (core) size. Several research groups have examined the effect of core size of AuNPs on surface density for large molecules using visible extinction spectroscopy and fluorescence spectrometry.[27,79,80] Their results indicate that smaller size particles may permit a higher molecular packing density. This dependency is especially true when the core size is less than about 30 nm in diameter, qualitatively consistent with our observation by ES-DMA. One possible explanation for this size dependency is the geometric curvature effect, which dictates that smaller particles (higher arc) can allow a higher packing density of macromolecules, such as BSA. Additionally, surface faceting, a characteristic associated with citrate stabilized AuNPs, may have a significant effect. Although the exact role is unconfirmed at this time, we speculate that the size and number of facets change with the core size and, if this is true, would be expected to have a measurable geometric effect on adsorbate density. For instance, nominally 60 nm AuNPs appear to have larger and fewer facets per particle relative to 10 nm AuNPs, based on electron microscopy images.[75] Table 2 summarizes the maximum surface density of BSA on AuNPs.

Table 2. Summary of Maximum Surface Density of BSA on AuNPs (σ_{max}) Estimated from Results Obtained by ES-DMA and Fluorescence Spectrometry

nominal size (nm)	σ_{max}, ES-DMA (nm^{-2})	σ_{max}, fluorescence (nm^{-2})
10	0.023 ± 0.003	0.005 ± 0.001
30	0.017 ± 0.002	0.010 ± 0.005
60	0.014 ± 0.002	0.008 ± 0.002

3.5. Adsorption Isotherms. In the previous sections, we probed the formation of BSA−AuNP conjugates and studied BSA surface density and conformation using complementary and orthogonal characterization approaches. Next, we employ and compare different methods to obtain the adsorption isotherm for BSA on AuNPs. By characterizing σ as a function of C_{BSA} at constant temperature, we can quantify the binding affinity for BSA on AuNPs by obtaining an equilibrium binding constant, K, which can be used, for example, as an important indicator in formulation design for nanomedicine applications.

Figure 6a shows the change in particle size measured as a function of C_{BSA}. Nominal 60 nm AuNPs are employed in this study. We normalize the change of hydrodynamic diameter ($\Delta d_{p,hz}$) and the change of aerodynamic diameter ($\Delta d_{p,m}$) relative to their maximum values at the highest C_{BSA} ($\Delta d_{p,hz,max}$ and $\Delta d_{p,m,max}$, respectively); in other words, $\Delta d_{p,hz}^* = \Delta d_{p,hz}/\Delta d_{p,hz,max}$ and $\Delta d_{p,m}^* = \Delta d_{p,m}/\Delta d_{p,m,max}$. As shown in Figure 6a, increasing C_{BSA} increases $\Delta d_{p,m}^*$ and $\Delta d_{p,hz}^*$ at lower C_{BSA} (<10 μmol/L), showing an increase in the amount of adsorbed BSA on the surface of the AuNPs. At C_{BSA} > 10 μmol/L, $\Delta d_p/\Delta d_{p,max}$ plateaus, indicating σ has attained a saturation level under these conditions. In our previous study,[50] DLS was found to provide better sensitivity than ES-DMA for probing the initial formation of SH-PEG5K−AuNP conjugates. In the present case, DLS and ES-DMA provide statistically identical results for $\Delta d_p/\Delta d_{p,max}$ versus C_{BSA}, indicating that these techniques have the same sensitivity to probe the conjugation of BSA and AuNPs.

Using eq 3, $\Delta d_{p,m}^*$ is converted to σ/σ_{max}, where σ_{max} is the maximum surface density of BSA calculated from the measurement results (plateau value). As shown in Figure 6b (diamond symbols), σ/σ_{max} reaches 90% when $C_{BSA} \approx 30$ μmol/L. Using the Langmuir adsorption model to obtain the equilibrium binding constant, K

$$K = \frac{1}{C_{BSA}[(\sigma_{max}/\sigma) - 1]} \tag{4}$$

As shown in Figure 6b (square symbols and line fit), a linear relationship between $1/[\sigma_{max}/\sigma - 1]$ and C_{BSA} exists with a slope, $K = 0.51 \times 10^6$ L/mol. This represents a relatively high binding constant (>10^4 L/mol) indicating a strong affinity for BSA on the AuNP surface, as would be expected if thiol-mediated bonding is involved (versus a purely physical adsorption mechanism). This value is consistent with previously reported values in the literature (≈1×10^6 L/mol[6,9]).

Figure 7a shows the adsorption isotherm measured by fluorescence assay using the same suspensions in Figure 6. Again, σ/σ_{max} reaches ≈90% when $C_{BSA} \approx 30$ μmol/L, consistent with the ES-DMA results above. Using eq 4, the equilibrium binding constant is estimated to be 0.62×10^6 L/mol. Figure 7b shows an adsorption isotherm obtained using a method based on ATR-FTIR. To quantify the relative surface density of BSA on AuNPs

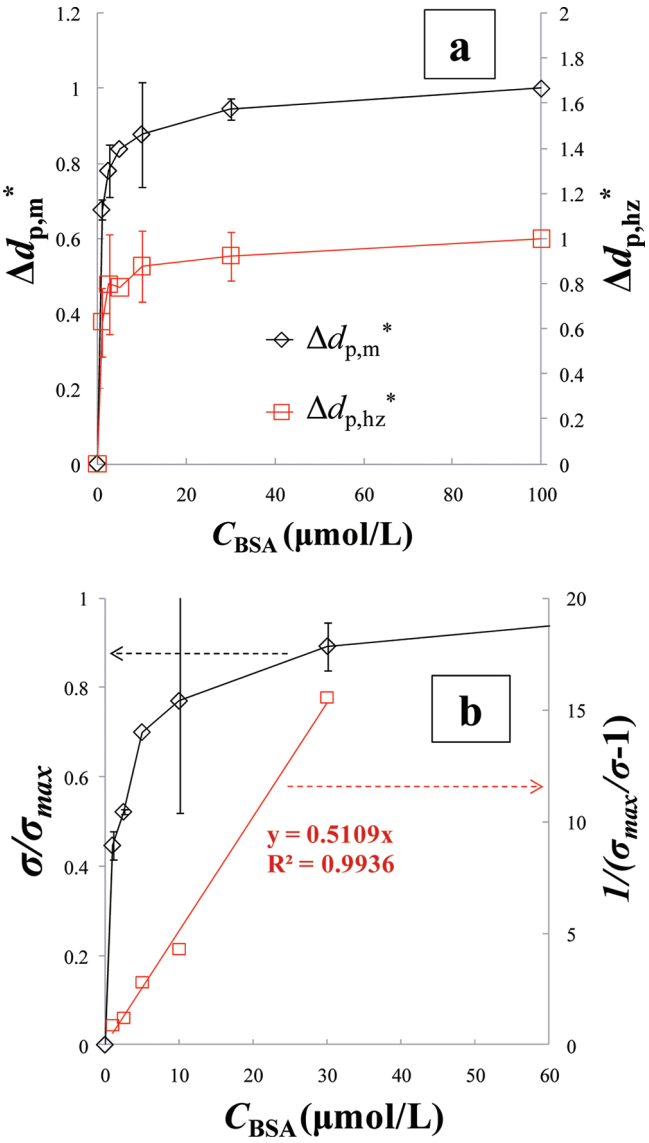

Figure 6. Adsorption isotherms for BSA on nominal 60 nm AuNPs obtained using physical measurement methods. Experimental temperature is 21 °C. (a) Dependence of the measured increase in particle size on C_{BSA}: $\Delta d_{p,m}^*$ (diamonds) and $\Delta d_{p,hz}^*$: (squares). (b) Calculated adsorption isotherm (diamonds and squares, based on ES-DMA) presented as fractional surface density; line is a guide to the eyes. Fit of data (line) to Langmuir adsorption equation. The slope K of the Langmuir fit gives the equilibrium binding constant. Error bars are one standard deviation based on two replicates measured under repeatability conditions. The pH during isotherm experiments was between 7.3 and 7.7.

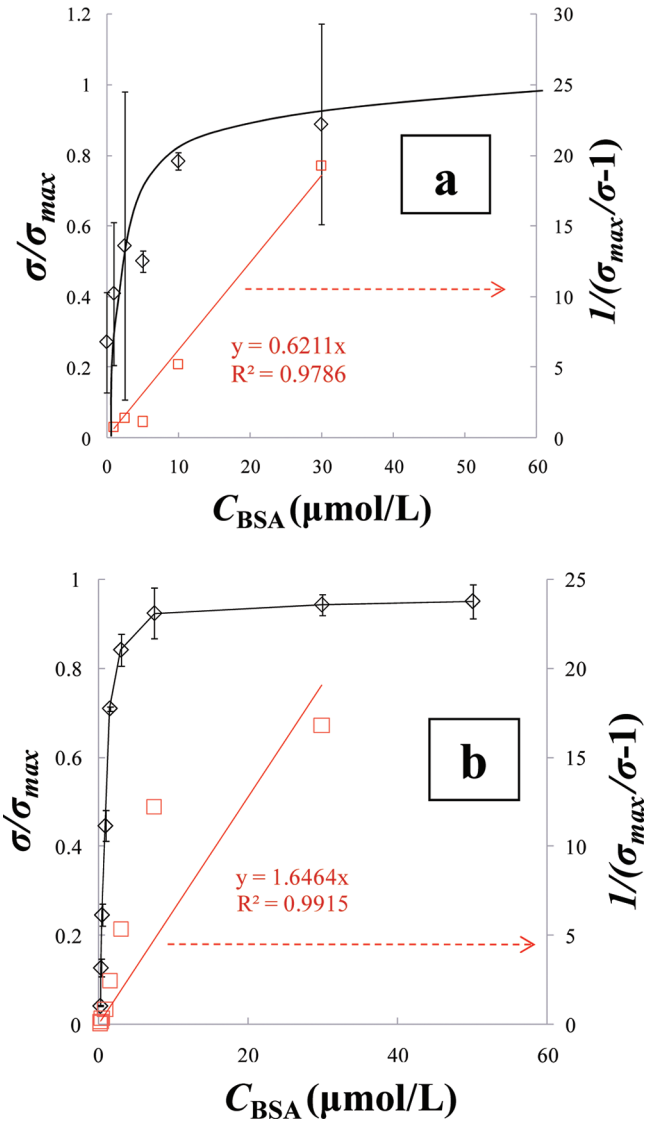

Figure 7. Adsorption isotherms (diamond symbols) for BSA on nominal 60 nm AuNPs obtained by spectroscopic methods. Experimental temperature is 21 °C. (a) Fluorescence spectrometry. (b) ATR-FTIR. Lines are a guide to the eyes. Data (square symbols) and fit to Langmuir model. Error bars represent one standard deviation for at least two replicate measurements. The slope K of the Langmuir fit is the equilibrium binding constant. The pH during isotherm measurements was between 7.0 and 7.4, but the initial native AuNP was unbuffered with a pH at 6.0.

by ATR-FTIR, we determine the peak heights at 1540 cm^{-1} (amide II) as a function of C_{BSA} in the flow cell and then normalize the peak heights by the maximum peak intensity to obtain σ/σ_{max}. This approach assumes that peak height scales proportionately with the adsorbed quantity of BSA; the results shown in Figure 7b indicate that σ/σ_{max} reaches ≈90% at a concentration of about 10 μmol/L. Using eq 4, an equilibrium binding constant of 1.65×10^6 L/mol is obtained, slightly higher than the values obtained by ES-DMA and fluorescence, but of similar magnitude (Figures 6b and 7a).

3.6. Effect of Adsorption and pH on BSA Secondary Structure. ATR-FTIR can be applied to investigate changes in the secondary structure of BSA after it is conjugated to the AuNP surface. Previously, IR spectroscopy has been used to investigate the interaction of BSA on flat gold surfaces,[71−73] using the amide I region to isolate changes in protein conformation. Differences in the amide bond orientation and the protein backbone are due to a varying secondary structure giving rise to various vibrational frequencies:[72] α-helix (1650−1655 cm^{-1}), β-sheet or β-turn (1663−1685 cm^{-1}), random chains (1644−1648 cm^{-1}), extended chains (1635−1639 cm^{-1}), and extended chains plus β-sheet (1621−1632 cm^{-1}). Therefore, the overall shape and

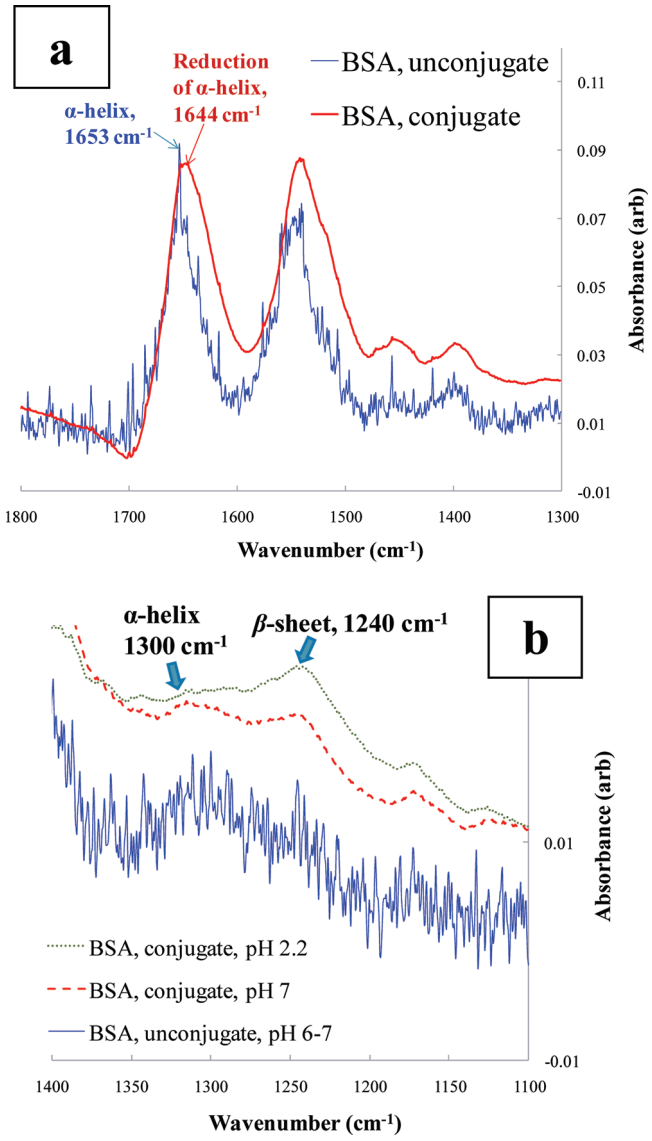

Figure 8. Comparison of ATR-FTIR spectra of unconjugated (free) BSA and BSA-AuNP conjugate: (a) amide I and amide II regions, pH between 6 and 7; (b) amide III region. The IR absorbance of unconjugated BSA is multiplied 30× for the purpose of comparison.

maxima of this amide I band are determined by the secondary structure of the protein. By deconvoluting the peak of the amide I region, Roach et al. studied changes in secondary structure of BSA following binding to different types of flat surfaces.[72] The authors determined that BSA is denatured by the interaction with an alkanethiol-functionalized Au film, a hydrophobic surface, in the process losing a large degree of their α-helix structure.

Presently we apply this approach to the analysis of BSA on spheroidal (but faceted) nominal 60 nm AuNPs. As shown in Figure 8a, the amide I peak for unconjugated BSA is centered at 1653 cm^{-1}, indicating that the principal secondary structure of free BSA at pH 7 is the α-helix form. After conjugation to AuNPs, the center of the amide I peak shifts down to 1644 cm^{-1}. The lower frequency regions represent less compact structures, as described above. Hence, the reduction of frequency indicates a change from the α-helix to more random and open chains. In addition to the peak frequency, the amide I band broadens asymmetrically to the right of the center frequency following conjugation, which indicates an increase in β-sheet content, random chains, or extended chains. These results, taken together, suggest that the secondary structure of BSA is changed in the process of conjugating with AuNPs.

Additional evidence for conformation change can be obtained by investigating the amide III region between 1200 and 1350 cm^{-1}. For BSA, the peak frequency at 1300 cm^{-1} is attributed to α-helix, and the peak frequency from 1235 to 1260 cm^{-1} corresponds to β-sheet.[81] Kaiden et al. investigated the denaturing of unbound BSA in solution, and they found not only that the frequency of amide I region was shifted to a lower value after denaturing but also that the peak intensities in the amide III region were altered. In our experiments, as shown in Figure 8b, after conjugation to AuNPs at neutral pH (red), the peak intensity at 1300 cm^{-1} was significantly decreased accompanied by the increase of the peak intensity at 1240 cm^{-1}, confirming the conformation of BSA conjugates are changed and transformed from α-helix to be β-sheet at the surface of the AuNP.

Looking into the effect of pH on the conformation of BSA conjugates, we saw a significant change in the amide III region by lowing pH from 7 (red, dashed) to 2.2 (green, dotted), even though the difference in the amide I region was less significant (Figure 4b and Figure S4 in Supporting Information). This result indicates possibly less α-helix presenting in the BSA conjugates at acidic pH relative to neutral pH, and a possible explanation may be the reduction of intermolecular electrostatic interaction, similar to the free BSA in different pH environments.[12,28,31,34,36,46,69]

Secondary structures of proteins are important to proteins functionality, in particular its biological activity. For instance, altering the secondary structure of proteins can significantly impact the corresponding enzyme activity.[82,83] Once proteins are bound to nanoparticles, the change of the secondary structure induced by the surface interaction may impact the corresponding enzyme activity of the protein−NP conjugate. For example, Wang et al. found a 36% decrease of enzyme activity when trypsin was immobilized on TiO_2, with a significant corresponding change in the secondary structure.[83] In the present work we use the BSA−AuNP conjugate as a model system and employ ATR-FTIR to investigate the change of BSA secondary structure following conjugate formation. The method proposed here is not limited to BSA−AuNPs and can be used to investigate other types of protein−NP systems. By characterizing the change of protein secondary structures under various conditions, one should be able to correlate this to the corresponding enzyme activity using in vitro and in vivo methods.

4. CONCLUSIONS

We have demonstrated that conjugation of BSA with AuNPs can be characterized quantitatively and qualitatively by applying complementary, and sometimes orthogonal, physical and spectroscopic methods. In the present study we use DLS, AFFF, ES-DMA, fluorescence spectrometry, and ATR-FTIR to obtain information regarding both molecular surface density and molecular conformation for BSA adsorbed onto AuNPs. For larger diameter AuNPs (nominally 60 nm) with a relatively lower contribution of scattered light arising from unbound BSA (i.e., a high γ ratio as defined previously), DLS exhibits reasonably good accuracy for probing the formation of BSA−AuNP

conjugates, and the results are consistent with those obtained by fractionation and high-resolution sizing via AFFF. For nominally smaller AuNP cores, interference from free BSA can skew results and complicate their interpretation unless additional steps are taken to remove the interference. The in situ physical characterization in the wet state (e.g., using DLS) explores the capacity to monitor the change of molecular conformation of BSA (or other globular proteins) on AuNPs under physiologically relevant conditions and in real time.

At similar BSA surface densities, we find a larger increase of BSA−AuNP size at pH < 2.5 than at a more basic pH values (pH 3.4−7.3), indicating a more expanded conformation under strongly acidic conditions corresponding to the so-called E or F forms of BSA. Moreover, we are able to exclude agglomeration as a source of particle size increase. When modifying pH between 3.4 and 7.3, the particle size measured by DLS is essentially constant, indicating the conformation of BSA conjugates is relatively stable over this pH range, and presumably represents the N form of BSA. This result is contrasted with free BSA, which is known to undergo at least two structural transformations over this pH range. ES-DMA has been used to characterize the particle size in the dry (aerosolized) state, where BSA surface density can be calculated from the measured change of aerosol size. The maximum surface density for BSA on AuNPs measured by ES-DMA and fluorescence spectrometry is dependent on the AuNP core size and consistent across characterization techniques. Adsorption isotherms obtained by multiple methods, including DLS, ES-DMA, fluorescence spectrometry, and ATR-FTIR, exhibit consistency across methods, with BSA surface density approaching 90% when C_{BSA} is ≈10−30 μmol/L. Using the Langmuir adsorption model to quantify the binding affinity, we obtain a surface binding constant for BSA on AuNPs ≈0.51×10^6 L/mol by ES-DMA, ≈0.62×10^6 L/mol by fluorescence assay, and 1.65×10^6 L/mol by ATR-FTIR. Thiol−gold binding at the interface may induce or modify the observed conformation change of BSA, and the secondary structure of BSA appears to be modified upon adsorption, resulting in more open structures and less α-helix structure. Factors that could potentially limit the applicability of this approach include the necessity to have robust binding between the adsorbates and the NP surface (in order to avoid desorption during the cleaning process required to remove excess adsorbate from the solution phase prior to fluorescence and ES-DMA measurements) and NP dimensions that approach the molecular size of the adsorbate (making it more difficult to separate the free and bound species and complicating the analysis of isotherms and size measurements).

Besides the adsorption of albumin on AuNPs, the proposed complementary characterization approach can also be used to study adsorption/desorption processes of other globular proteins onto/from various types of nanoparticle systems. Through the quantitative study of particle−protein interactions, as demonstrated in this paper, parameters such as equilibrium binding constants and adsorption/desorption rate constants can be obtained and then used to improve the formulation design and quality assurance of nanomedicine products. The work presented here provides proof of concept and demonstrates the efficacy of the complementary characterization approach for the investigation of protein conjugation in nanoparticle systems. This work also serves as a template for the application of commonly used methods, such as DLS and fluorescence spectrometry, for investigating the interaction of nanoparticles with proteins and other surface-active molecular species.

■ ASSOCIATED CONTENT

Ⓢ Supporting Information. Additional information on characterizing BSA-conjugated AuNP. This material is available free of charge via the Internet at http://pubs.acs.org.

■ AUTHOR INFORMATION

Corresponding Author
*E-mail: vince.hackley@nist.gov.

■ ACKNOWLEDGMENT

The authors acknowledge Dr. Anil Patri of the National Cancer Institute's Nanotechnology Characterization Laboratory for helpful discussions in advance of the present work. The authors thank Dr. Richard Gates at the National Institute of Standards and Technology (NIST) for his assistance with the ATR-FTIR measurements and Ms. Melissa Davila-Morris, a Summer Undergraduate Research Fellow at NIST, for her assistance with sample preparation for the fluorescence and ATR-FTIR measurements. In addition, the authors also thank Dr. Julian Taurozzi, Dr. Robert Cook, and Suvajyoti Guha at NIST for the review and suggestions to the manuscript.

■ REFERENCES

(1) The findings and conclusions in this article have not been formally disseminated by the Food and Drug Administration and should not be construed to represent any Agency determination or policy.

(2) Paciotti, G.; Li, Q.; Simpson, B.; Soltesiak, K.; Meyer, L.; Davis, N.; Tamarkin, L. *Eur. Cytokine Network* **1998**, *9* (3), 536.

(3) Paciotti, G. F.; Myer, L. D.; Kim, T. H.; Wang, S.; Alexander, H. R.; Weinreich, D.; Tamarkin, L. *Clin. Cancer Res.* **2001**, *7* (11), 3673S–3674S.

(4) Paciotti, G. F.; Myer, L.; Weinreich, D.; Goia, D.; Pavel, N.; McLaughlin, R. E.; Tamarkin, L. *Drug Delivery* **2004**, *11* (3), 169–183.

(5) Paciotti, G. F.; Kingston, D. G. I.; Tamarkin, L. *Drug Dev. Res.* **2006**, *67* (1), 47–54.

(6) Brewer, S. H.; Glomm, W. R.; Johnson, M. C.; Knag, M. K.; Franzen, S. *Langmuir* **2005**, *21* (20), 9303–9307.

(7) Wangoo, N.; Suri, C. R.; Shekhawat, G. *Appl. Phys. Lett.* **2008**.

(8) Eck, W.; Craig, G.; Sigdel, A.; Ritter, G.; Old, L. J.; Tang, L.; Brennan, M. F.; Allen, P. J.; Mason, M. D. *ACS Nano* **2008**, *2* (11), 2263–2272.

(9) Lacerda, S. H. D.; Park, J. J.; Meuse, C.; Pristinski, D.; Becker, M. L.; Karim, A.; Douglas, J. F. *ACS Nano* **2010**, *4* (1), 365–379.

(10) Lynch, I.; Dawson, K. A. *Nano Today* **2008**, *3* (1−2), 40–47.

(11) Dobrovolskaia, M. A.; Patri, A. K.; Zheng, J. W.; Clogston, J. D.; Ayub, N.; Aggarwal, P.; Neun, B. W.; Hall, J. B.; Mcneil, S. E. *Nanomed.-Nanotechnol. Biol. Med.* **2009**, *5* (2), 106–117.

(12) Carter, D. C.; Ho, J. X. *Adv. Protein Chem.* **1994**, *45* (45), 153–203.

(13) Ho, J. X.; Holowachuk, E. W.; Norton, E. J.; Twigg, P. D.; Carter, D. C. *Eur. J. Biochem.* **1993**, *215* (1), 205–212.

(14) Goodman, D. S. *J. Am. Chem. Soc.* **1958**, *80* (15), 3892–3898.

(15) Ao, L. M.; Gao, F.; Pan, B. F.; Cui, D. X.; Gu, H. C. *Chin. J. Chem.* **2006**, *24* (2), 253–256.

(16) Chadborn, N.; Bryant, J.; Bain, A. J.; O'Shea, P. *Biophys. J.* **1999**, *76* (4), 2198–2207.

(17) Moulin, A. M.; O'Shea, S. J.; Badley, R. A.; Doyle, P.; Welland, M. E. *Langmuir* **1999**, *15* (26), 8776–8779.

(18) Figge, J.; Rossing, T. H.; Fencl, V. *J. Lab. Clin. Med.* **1991**, *117* (6), 453–467.

(19) Porter, D.; Sriram, K.; Wolfarth, M.; Jefferson, A.; Schwegler-Berry, D.; Andrew, M.; Castranova, V. *Nanotoxicology* **2008**, *2* (3), 144–154.
(20) Sager, T. M.; Porter, D. W.; Robinson, V. A.; Lindsley, W. G.; Schwegler-Berry, D. E.; Castranova, V. *Nanotoxicology* **2007**, *1* (2), 118–129.
(21) Bihari, P.; Vippola, M.; Schultes, S.; Praetner, M.; Khandoga, A. G.; Reichel, C. A.; Coester, C.; Tuomi, T.; Rehberg, M.; Krombach, F. *Part. Fibre Toxicol.* **2008**.
(22) Ji, Z.; Jin, X.; George, S.; Xia, T.; Meng, H.; Wang, X.; Suarez, E.; Zhang, H.; Hoek, E. M. V.; Godwin, H.; Nel, A. E.; Zink, J. I. *Environ. Sci. Technol.* **2010**, DOI 10.1021/es100417s.
(23) Schulze, C.; Kroll, A.; Lehr, C. M.; Schafer, U. F.; Becker, K.; Schnekenburger, J.; Isfort, C. S.; Landsiedel, R.; Wohlleben, W. *Nanotoxicology* **2008**, *2* (2), 51–U17.
(24) Tantra, R.; Tompkins, J.; Quincey, P. *Colloids Surf., B* **2010**, *75* (1), 275–281.
(25) Song, L. Sorption of Bovine Serum Albumin on Nano and Bulk Oxide Particles. MS Dissertation, University of Massachusetts—Amherst, 2009.
(26) Estey, T.; Kang, J.; Schwendeman, S. P.; Carpenter, J. F. *J. Pharm. Sci.* **2006**, *95* (7), 1626–1639.
(27) Teichroeb, J. H.; Forrest, J. A.; Jones, L. W. *Eur. Phys. J. E: Soft Matter Biol. Phys.* **2008**, *26* (4), 411–415.
(28) Peters, T. *Adv. Protein Chem.* **1985**, *37*, 161–245.
(29) Era, S.; Sogami, M. *J. Pept. Res.* **1998**, *52* (6), 431–442.
(30) Hirayama, K.; Akashi, S.; Furuya, M.; Fukuhara, K. *Biochem. Biophys. Res. Commun.* **1990**, *173* (2), 639–646.
(31) Lee, C. T.; Smith, K. A.; Hatton, T. A. *Biochemistry* **2005**, *44* (2), 524–536.
(32) Brown, J. R. *Fed. Proc.* **1975**, *34* (3), 591.
(33) Cannistraro, S.; Sacchetti, F. *Phys. Rev. A* **1986**, *33* (1), 745–746.
(34) Khan, M. Y. *Biochem. J.* **1986**, *236* (1), 307–310.
(35) Putnam, F. W. *The Plasma Proteins*, 2nd ed.; Academic Press: New York, 1975; Vol. 1.
(36) Harrington, W. F.; Johnson, P.; Ottewill, R. H. *Biochem. J.* **1956**, *62* (4), 569–582.
(37) Katchalski, E.; Benjamin, G. S.; Gross, V. *J. Am. Chem. Soc.* **1957**, *79* (15), 4096–4099.
(38) Cedervall, T.; Lynch, I.; Lindman, S.; Berggard, T.; Thulin, E.; Nilsson, H.; Dawson, K. A.; Linse, S. *Proc. Natl. Acad. Sci. U.S.A.* **2007**, *104* (7), 2050–2055.
(39) Fujiwara, K.; Watarai, H.; Itoh, H.; Nakahama, E.; Ogawa, N. *Anal. Bioanal. Chem.* **2006**, *386* (3), 639–644.
(40) Housni, A.; Ahmed, M.; Liu, S. Y.; Narain, R. *J. Phys. Chem. C* **2008**, *112* (32), 12282–12290.
(41) Krasovskii, V. I.; Nagovitsyn, I. A.; Chudinova, G. K.; Savranskii, V. V.; Karavanskii, V. A. *Bull. Lebedev Phys. Inst.* **2007**, *34* (11), 321–324.
(42) Pan, B. F.; Cui, D. X.; Xu, P.; Li, Q.; Huang, T.; He, R.; Gao, F. *Colloids Surf., A* **2007**, *295* (1−3), 217–222.
(43) Reilly, J. P. O.; Fisk, J. D.; Rooth, M.; Perkins, E.; Shaw, A. M. *Phys. Chem. Chem. Phys.* **2007**, *9* (3), 344–345.
(44) Nakata, S.; Kido, N.; Hayashi, M.; Hara, M.; Sasabe, H.; Sugawara, T.; Matsuda, T. *Biophys. Chem.* **1996**, *62* (1−3), 63–72.
(45) Silin, V.; Weetall, H.; Vanderah, D. J. *J. Colloid Interface Sci.* **1997**, *185* (1), 94–103.
(46) Shang, L.; Wang, Y. Z.; Jiang, J. G.; Dong, S. J. *Langmuir* **2007**, *23* (5), 2714–2721.
(47) MacCuspie, R. I.; Allen, A. J.; Hackley, V. A. *Nanotoxicology* **2010**, DOI 10.3109/17435390.2010.504311.
(48) Pease, L. F.; Tsai, D. H.; Zangmeister, R. A.; Zachariah, M. R.; Tarlov, M. J. *J. Phys. Chem. C* **2007**, *111* (46), 17155–17157.
(49) Tsai, D. H.; Zangmeister, R. A.; Pease, L. F.; Tarlov, M. J.; Zachariah, M. R. *Langmuir* **2008**, *24* (16), 8483–8490.
(50) Tsai, D. H.; Delrio, F. W.; MacCuspie, R. I.; Cho, T. J.; Zachariah, M. R.; Hackley, V. A. *Langmuir* **2010**, *26* (12), 10325–10333.
(51) Pease, L. F.; Lipin, D. I.; Tsai, D. H.; Zachariah, M. R.; Lua, L. H. L.; Tarlov, M. J.; Middelberg, A. P. J. *Biotechnol. Bioeng.* **2009**, *102* (3), 845–855.
(52) Corrigan, T. D.; Guo, S.; Phaneuf, R. J.; Szmacinski, H. *J. Fluoresc.* **2005**, *15* (5), 777–784.
(53) Guo, S. H.; Tsai, S. J.; Kan, H. C.; Tsai, D. H.; Zachariah, M. R.; Phaneuf, R. J. *Adv. Mater.* **2008**, *20* (8), 1424.
(54) Tsai, D. H.; Hawa, T.; Kan, H. C.; Phaneuf, R. J.; Zachariah, M. R. *Nanotechnology* **2007**.
(55) Hackley, V. A.; Clogston, J. D. NIST-NCL Joint Assay Protocol PCC-1.
(56) Certain commercial equipment, instruments, or materials are identified in this report in order to specify the experimental procedure adequately. Such identification is not intended to imply recommendation or endorsement by the National Institute of Standards and Technology or the Department of Health and Human Services nor is it intended to imply that the materials or equipment identified are necessarily the best available for the purpose.
(57) Pease, L. F., III; Tsai, D. H.; Hertz, J. L.; Zangmeister, R. A.; Zachariah, M. R.; Tarlov, M. J. *Langmuir* **2010**, *26* (13), 11384–11390.
(58) Pease, L. F.; Elliott, J. T.; Tsai, D. H.; Zachariah, M. R.; Tarlov, M. J. *Biotechnol. Bioeng.* **2008**, *101* (6), 1214–1222.
(59) Tsai, D. H.; Pease, L. F.; Zangmeister, R. A.; Tarlov, M. J.; Zachariah, M. R. *Langmuir* **2009**, *25* (1), 140–146.
(60) Cho, T. J.; Hackley, V. A. *Anal. Bioanal. Chem.* **2010**10.1007/s00216-010-4133-6.
(61) ISO 13321:1996(E). Particle size analysis - Photon correlation spectroscopy, 1996.
(62) ISO 22412:2008, 2008.
(63) Kaufman, E. D.; Belyea, J.; Johnson, M. C.; Nicholson, Z. M.; Ricks, J. L.; Shah, P. K.; Bayless, M.; Pettersson, T.; Feldoto, Z.; Blomberg, E.; Claesson, P.; Franzen, S. *Langmuir* **2007**, *23* (11), 6053–6062.
(64) Kozak, M. *J. Appl. Crystallogr.* **2005**, *38*, 555–558.
(65) Cummins, H. Z. *Photon Correlation Spectroscopy and Velocimetry*; Plenum Press: New York, 1977.
(66) Schurr, J. M. *CRC Crit. Rev. Biochem.* **1977**, *4* (4), 371–431.
(67) http://www.robinwood.com/Catalog/Technical/Gen3DTuts/Gen3DPages/RefractionIndexList.html, 2010.
(68) Drexler, K. E. *Proc. Natl. Acad. Sci. U.S.A.* **1981**, *78* (9), 5275–5278.
(69) Kun, R.; Szekeres, M.; Dekany, I. *J. Therm. Anal. Calorim.* **2009**, *96* (3), 1009–1017.
(70) Li, Y.; Lee, J.; Lal, J.; An, L.; Huang, Q. *J. Phys. Chem. B* **2008**, *112* (12), 3797–3806.
(71) Lenk, T. J.; Horbett, T. A.; Ratner, B. D.; Chittur, K. K. *Langmuir* **1991**, *7* (8), 1755–1764.
(72) Roach, P.; Farrar, D.; Perry, C. C. *J. Am. Chem. Soc.* **2005**, *127* (22), 8168–8173.
(73) Smith, J. R.; Cicerone, M. T.; Meuse, C. W. *Langmuir* **2009**, *25* (8), 4571–4578.
(74) Mulholland, G. W.; Donnelly, M. K.; Hagwood, C. R.; Kukuck, S. R.; Hackley, V. A.; Pui, D. Y. H. *J. Res. Natl. Inst. Stand. Technol.* **2006**, *111* (4), 257–312.
(75) National Institute of Standards and Technology (NIST) Report of Investigation, Reference Materials 8011−8013.
(76) http://www.its.bldrdoc.gov/fs-1037/Federal Standard 1037C, 2007.
(77) Vigil, R. D.; Ziff, R. M. *J. Chem. Phys.* **1989**, *91* (4), 2599–2602.
(78) Adamczyk, Z.; Barbasz, J.; Ciesla, M. *Langmuir* **2010**, *26* (14), 11934–11945.
(79) Cederquist, K. B.; Keating, C. D. *ACS Nano* **2009**, *3* (2), 256–260.
(80) Hill, H. D.; Millstone, J. E.; Banholzer, M. J.; Mirkin, C. A. *ACS Nano* **2009**, *3* (2), 418–424.
(81) Kaiden, K.; Matsui, T.; Tanaka, S. *Appl. Spectrosc.* **1987**, *41* (2), 180–184.
(82) Petkova, G. A.; Kral, V. *Bioorg. Med. Chem.* **2010**, *18* (18), 6651–6656.
(83) Wang, W. R.; Zhu, R. R.; Xiao, R.; Liu, H.; Wang, S. L. *Biol. Trace Elem. Res.* **2010**, DOI 10.1007/s12011-010-8823-x.